HHS Public Access

Author manuscript

Magn Reson Med. Author manuscript; available in PMC 2018 February 01.

Published in final edited form as:

Magn Reson Med. 2017 February ; 77(2): 855–863. doi:10.1002/mrm.26131.

Quantitative Assessment of the Effects of Water Proton Concentration and Water T_1 Changes on Amide Proton Transfer (APT) and Nuclear Overhauser Enhancement (NOE) MRI: The Origin of the APT Imaging Signal in Brain Tumor

Dong-Hoon Lee[1], **Hye-Young Heo**[1], **Kai Zhang**[1], **Yi Zhang**[1], **Shanshan Jiang**[1], **Xuna Zhao**[1], and **Jinyuan Zhou**[1,2,*]

[1]Division of MR Research, Department of Radiology, Johns Hopkins University School of Medicine, Baltimore, Maryland, USA

[2]F.M. Kirby Research Center for Functional Brain Imaging, Kennedy Krieger Institute, Baltimore, Maryland, USA

Abstract

Purpose—To quantify pure CEST-related APT and NOE signals in a rat glioma model and to investigate the mixed effects of water content and water T_1 on APT and NOE imaging signals.

Methods—Eleven U87 tumor-bearing rats were scanned at 4.7 T. A relatively accurate mathematical approach, based on extrapolated semi-solid magnetization-transfer reference signals, was used to remove the concurrent effects of direct water saturation and semi-solid magnetization-transfer. Pure APT and NOE signals, in addition to the commonly used magnetization-transfer-ratio-asymmetry at 3.5 ppm, $MTR_{asym}(3.5ppm)$, were assessed.

Results—The measured APT signal intensity of the tumor (11.06%, much larger than the value reported in the literature) was the major contributor (about 80.6%) to the $MTR_{asym}(3.5ppm)$ contrast between the tumor and the contralateral brain region. Both the water content ([water proton]) and water T_1 (T_{1w}) were increased in the tumor, but there were no significant correlations between APT, NOE, or $MTR_{asym}(3.5ppm)$ signals and T_{1w}/[water proton].

Conclusion—The effect of increasing T_{1w} on the CEST signal in the tumor was mostly canceled out by the effect of increasing water content, and the observed APT-weighted hyperintensity in the tumor should be dominated by the increased amide proton concentration.

Keywords

CEST; APT; NOE; MT; water content; water T_1

*Corresponding author: Jinyuan Zhou, Ph.D., Division of MR Research, Department of Radiology, Johns Hopkins University, School of Medicine, 600 N. Wolfe Street, Park 336, Baltimore, MD 21287, USA, Phone: (+1-410) 955-7491, Fax: (+1-410) 614-1977, jzhou@mri.jhu.edu.

INTRODUCTION

Chemical exchange-dependent saturation transfer (CEST) imaging provides an important contrast mechanism for molecular MRI (1). Thus far, numerous promising CEST applications have been exploited in different ways to detect various compounds, including proteins (2–5), glycosaminoglycan (6, 7), glutamate (8, 9), and creatine (10). In addition to these endogenous biomolecules, many kinds of exogenous CEST agents (paramagnetic and diamagnetic) have been introduced, such as paramagnetic lanthanide complexes (11–13), some x-ray contrast agents (such as iopamidol and iopromide) (14, 15), and glucose (16–19). Among them, amide proton transfer (APT) imaging, using mobile proteins and peptides in tissue, has been successfully used to detect tumors (increasing mobile protein and peptide concentration) (20–24), to assess treatment effects of tumors using radiotherapy, chemotherapy, or high-intensity focused ultrasound (25–28), and to detect strokes (decreasing pH) (29–34).

To quantify the CEST effects, the magnetization transfer ratio (MTR = 1 − S_{sat}/S_0, where S_{sat} and S_0 are the image intensities with and without radiofrequency (RF) saturation) asymmetry analysis with respect to the water resonance has been widely used in various applications. For example, for APT imaging at 3.5 ppm downfield from the water frequency, one has (2, 3):

$$\begin{aligned} MTR_{asym}(3.5\ ppm) &= MTR(+3.5\ ppm, \text{label}) - MTR(-3.5\ ppm, \text{reference}) \\ &= \frac{S_{sat}(-3.5\ ppm, \text{reference}) - S_{sat}(+3.5\ ppm, \text{label})}{S_0} \end{aligned} \quad [1]$$

Although this analysis method can effectively remove the concurrent effects of direct water saturation (spillover) and semi-solid magnetization transfer (MT), the quantified MTR_{asym}(3.5ppm) signal intensity is inevitably mixed with the upfield nuclear Overhauser enhancement (NOE) effect at −3.5 ppm relative to the water resonance (35–40). Thus, under the zero-order approximation, one has (2, 3):

$$\begin{aligned} MTR_{asym}(3.5\ ppm) &\approx APTR + MTR'_{asym}(3.5\ ppm) \\ &\approx APTR - [NOER^{mobile}(-3.5\ ppm) + NOER^{relativly\ mobile}(-3.5\ ppm)] \\ &= APT^{\#} - NOE^{\#} \end{aligned} \quad [2]$$

where APTR is the proton transfer ratio for the amide protons and MTR'_{asym}(3.5ppm) includes various non-APT effects asymmetrical at ±3.5 ppm from the water resonance, such as the upfield NOE effects of mobile and relatively less mobile polypeptides, lipids, and metabolites in tissue, quantified by the NOE-based MT ratio (NOER) (41). Thus, the MTR_{asym}(3.5ppm) images calculated by Eq. [2] are usually called APT-weighted images.

According to the theory, the APTR can be approximately described as (42):

$$APTR = \frac{K_{sw} \cdot T_{1w} \cdot [Amide\ proton]}{[Water\ proton]} \cdot \left(1 - e^{-\frac{t_{sat}}{T_{1w}}}\right) \quad [3]$$

where K_{sw} is the pH-dependent amide proton exchange rate ($K_{sw} = 5.57\times10^{pH-6.4}$ in the rat brain (3)), T_{1w} is the water longitudinal relaxation time (excluding the contribution of the mobile amide protons), [ ] indicates the concentration of amide protons or water protons, and t_{sat} is the applied RF saturation time. As described in Eq. [3], the APT signal intensity depends on the mobile amide proton concentration, the amide proton exchange rate (depending on tissue pH), and several other tissue and experimental parameters (apparently proportional to T_{1w} and inversely proportional to [water proton]). To better understand the APT-MRI contrast mechanism, one extremely important issue is to assess whether and how T_{1w} and the water proton concentration affect the observed APT signal intensity and image contrast.

In this study, we quantified the downfield APT, the upfield NOE, and the MTR_{asym}(3.5ppm) signal features in rat brain tumor model. We used extrapolated semi-solid MT reference (EMR) signals at ±3.5 ppm from the water resonance, a relatively accurate approach that was recently introduced for the quantification of APT and NOE effects (43, 44). The goals of this study were two-fold: (i) to investigate the APT, NOE, and MTR_{asym}(3.5ppm) signal features and their relationships in malignant glioma in order to demonstrate the reliability and validity of MTR_{asym}(3.5ppm) as an APT imaging metric for daily clinical applications; and (ii) to investigate the correlations between APT signal intensities and other tissue parameters (T_{1w} and [water proton]) in order to elucidate the possible factors that affect the APT imaging mechanism.

METHODS

MRI Data Acquisition

All experiments, as well as animal care, were approved by the Johns Hopkins Animal Care and Use Committee. All imaging experiments were performed on a 4.7 T animal MRI system (Bruker Biospin, Billerica, MA), with a 7 cm coil for RF transmission and a 2.5 cm surface coil for signal reception. Eleven U87 glioma-bearing male nude rats (0.2 million cells implanted for each rat, post-implantation days 12–14) were scanned. High-resolution coronal T_2-weighted images were acquired around the lesion in the brain, with the following parameters: repetition time (TR) = 3 sec; echo time (TE) = 64 msec; five slices with no gap; slice thickness = 1.5 mm; field of view (FOV) = 40/32 × 32 mm^2; matrix size = 256/192 × 192; number of averages (NA) = 2. Several quantitative MRI datasets were then acquired (26). For T_{1w}^{obs} mapping, based on an inversion recovery, spin-echo, echo-planar imaging (EPI) sequence, seven inversion recovery times (0.05, 0.3, 0.6, 1.2, 1.8, 2.5, and 3.5 sec) were used with a pre-delay time = 3 sec; TE = 30 msec; and NA = 4. For T_{2w}^{obs} mapping, a spin-echo EPI sequence with seven TEs (30, 40, 50, 60, 70, 80, and 90 msec); TR = 3 sec; and NA = 4 was used. Apparent diffusion coefficient (ADC) maps were obtained, using an isotropic, pulsed-gradient, spin-echo diffusion sequence with seven b-values (0, 166.7, 333.3, 500, 666.7, 833.3, and 1000 s/mm^2); TR = 3 sec; TE = 80 msec; and NA = 8. Cerebral blood flow (CBF) maps were obtained, using the standard arterial spin labeling technique with 3-sec labeling at a distance of 15 mm away from the imaging plane; TR = 6 sec; TE = 28.6 msec; and NA = 16.

CEST datasets were acquired using a fat-suppressed, spin-echo EPI pulse sequence (40, 45), with a long continuous-wave RF saturation pulse and a single-shot EPI readout (TR = 10 sec; TE = 30 msec; coronal; single slice; matrix size = 64 × 64 mm^2; FOV = 32 × 32 mm^2; slice thickness = 1.5 mm; RF saturation power = 1.3 μT; and RF saturation time = 4 sec). Z-spectra with 61 frequency offsets were acquired as follows. A control image (S_0 image) and saturation images, with offsets from +15 to −15 ppm at intervals of 0.5 ppm, were obtained for MT modeling and quantification analysis. For B_0-field inhomogeneity corrections, water saturation shift referencing (WASSR) (46) Z-spectra, with 26 frequency offsets, were acquired from +0.6 to −0.6 ppm at intervals of 0.05 ppm, using 0.5-μT RF saturation power. In addition, high signal-to-noise ratio APT images were acquired using two frequency offsets (±3.5 ppm) and 16 signal averages.

Data Processing and Fitting

Figure 1 shows the flow chart of data processing procedures. Prior to the fitting, the Z-spectrum within a range of ±15 ppm, normalized by the unsaturated image, was subjected to B_0-field correction, using the WASSR method (46). The B_0-corrected Z-spectrum was fitted to Henkelman's two-pool MT model with a super-Lorentzian lineshape (47, 48). The EMR fitting was performed by the similar procedures based on the recently published papers (43, 44). To avoid possible CEST and NOE contributions around the water resonance to conventional MT modeling, we performed the fitting within limited data points of frequency offsets +15 ~ +7 ppm in B_0-corrected $Z_{+15 \sim -15\ ppm}$. By fitting of the modified offset range, the four independent MT model parameters (R, $RM_{0m}T_{1w}$, T_{1w}/T_{2w}, T_{2m}) were obtained using the nonlinear least-squares fitting approach. The R is the exchange rate between the bulk water pool and the semi-solid macromolecule pool; M_{0m} is the equilibrium magnetizations of the semi-solid macromolecular pool; T_{1w} and T_{2w} are the longitudinal and transverse relaxation times of the free water proton pool, respectively; T_{2m} is the transverse relaxation time of the semi-solid macromolecular proton pool. In this fitting procedure, the equilibrium magnetization of the bulk water pool was normalized to 1, and the longitudinal relaxation time of the semi-solid macromolecular proton pool, which is not sensitive to the fitting procedure (47, 48), was fixed to be one second. Moreover, the water longitudinal relaxation parameter, T_{1w}, and the observed value obeyed the following equation (47):

$$T_{1w}=T_{1w}^{obs}\left[1+\left(\frac{RM_{0m}T_{1w}\left(\frac{1}{T_{1m}}-\frac{1}{T_{1w}^{obs}}\right)}{\left(\frac{1}{T_{1m}}-\frac{1}{T_{w}^{obs}}\right)+R}\right)\right] \quad [4]$$

Acquired T_{1w}^{obs} and T_{2w}^{obs} values from the longitudinal and transverse relaxation maps (see below) were also combined to improve the fitting of the MT model parameters. The fitting results using the estimated MT model parameters were evaluated by the root of the sum of the squared differences between the fitted and experimental data, and goodness of fit (R^2) was calculated on a pixel-wise basis. Finally, $APT^{\#}$ and $NOE^{\#}$ were calculated by subtracting the experimental data from the EMR data.

For other MRI parameters, the T_{1w}^{obs} map and T_{2w}^{obs} map were fitted using the following equations: $I = I_0 + A \exp(-TI/T_{1w}^{obs})$ and $I = I_0 \exp(-TE/T_{2w}^{obs})$. The [water proton] map was obtained based on the I_0 values, together with the T_{1w}^{obs} fitting. To minimize the T_2 effect, the [water proton] map was corrected with an $\exp(-TE/T_{2w}^{obs})$ factor. Note that the absolute [water proton] quantification is a little difficult by MRI, so only the relative water proton concentration (tumor compared to contralateral brain) was reported in this study. The ADC map was fitted using the following equation: $I = I_0 \exp(-b\ ADC)$. The CBF map was reconstructed from images with and without labeling.

Quantitative Image Analysis and Statistical Analysis

Two regions of interest (ROIs) from the contralateral and tumor regions were carefully drawn on the ADC map. Image contrast values were calculated by signal intensity differences between the contralateral and the tumor regions. Statistical differences in signal intensities and image contrasts among the contralateral and the tumor regions were analyzed by a one-way analysis of variance test, followed by the Tukey's post-hoc test. The level of significance was set at $p < 0.05$. Correlations of $APT^{\#}$, $NOE^{\#}$, and $MTR_{asym}(3.5ppm)$ with T_{1w}/[water proton] were performed. For the correlation analysis, the Pearson's correlation coefficients and *p* values were acquired. The strengths of the correlations were set at $r > 0.70$ (very strong), 0.69 to 0.40 (strong), 0.39 to 0.30 (moderate), 0.29 to 0.20 (weak), and < 0.19 (none or negligible). All image data processing was performed using MATLAB R2013b (The MathWorks, Inc., Natick, MA), and all statistical analyses were performed using the statistical package SPSS for Windows (Version 18, Chicago, IL).

RESULTS

Figure 2a and b shows the average, two-pool, semi-solid MT-fitted Z_{EMR} curves (based on $Z_{+15 \sim +7\ ppm}$) and experimentally measured Z-spectra ($Z_{+15 \sim -15\ ppm}$) from the contralateral and tumor regions. Table 1 indicates the calculated MT model parameters (R, $RM_{0m}T_{1w}$, T_{1w}/T_{2w}, T_{2m}) and the R^2 goodness-of-fit values. Notably, both Z_{EMR} curves for the contralateral and tumor regions had higher signal intensities than the measured Z-spectra for all frequency offsets, particularly those around the water resonance, due to the downfield APT and other CEST and upfield NOE contributions.

The calculated downfield $APT^{\#}$ and other $CEST^{\#}$, upfield $NOE^{\#}$, and $MTR_{asym}(3.5ppm)$ signal features as a function of frequency offsets are shown in Fig. 2c and d. Based on the EMR method, the specific, large $APT^{\#}$ signals peaked at roughly 3.5 ppm downfield from water, and the amine $CEST^{\#}$ signals peaked at roughly 2 ppm downfield from water were observed in both regions (particularly noticeable in the tumor region). In addition, there were large $NOE^{\#}$ signals that appeared at roughly −2 to −5 ppm upfield from water in the tumor region and in a wider offset range (outside of −5 ppm) in the contralateral region. According to Fig. 2c, it is clear that the $APT^{\#}$ contrast between the tumor and the contralateral brain region was most dominant at 3.5 ppm, and the contrast was close to zero as the frequency offset increase. On the contrary, the $NOE^{\#}$ contrast was small at 3.5 ppm and increased with frequency offsets (> 5 ppm). Based on the MTR asymmetry analysis (defined by Eq. [1]), the absolute MTR_{asym} signal intensity values were reduced due to the upfield NOE

contributions. The MTR_{asym} curves clearly peaked at roughly 2 and 3.5 ppm downfield from water (particularly in the tumor region), and became negative for large frequency offsets (particularly in the contralateral region, representing a significant influence of the upfield NOE effects). Moreover, the MTR_{asym} contrast between the tumor and the contralateral brain region at 3.5 ppm was most dominant (about 80.6%) due to the downfield large $APT^{\#}$. These results clearly show that the APT effect contributes the most to the tumor MTR_{asym} contrast at 3.5 ppm.

Figure 3 shows the calculated $APT^{\#}$, $NOE^{\#}$, and MTR_{asym}(3.5ppm) signal intensities, and image contrasts (signal intensities in the tumor region - signal intensities in the contralateral region). Several important results can be summarized as follows. (i) In the U87 tumor xenografts, typically without spontaneous necrosis (49), the calculated $APT^{\#}$ signal intensity (11.06 ± 0.46%) of the tumor was much larger than the value reported previously (25), and significantly higher than that of the contralateral (6.33 ± 0.68%; $p < 0.001$). The $APT^{\#}$ image contrast between the tumor and the contralateral regions was as large as 4.73 ± 0.86%. (ii) The quantified $NOE^{\#}$ signal intensities were as large as 6.93% (tumor) and 8.08% (contralateral), and showed no significant difference between the contralateral and tumor regions. The $NOE^{\#}$ image contrast between the contralateral and tumor regions was negative and small (−1.14 ± 0.92%). (iii) The quantified MTR_{asym}(3.5ppm) signal intensity became smaller than the $APT^{\#}$ signal intensity, due to contamination from the upfield NOE effects (based on Eq. [2]). The tumor xenograft had positive MTR_{asym}(3.5ppm) signal intensity (4.12 ± 1.02%). This is because we used relatively higher RF saturation power (1.3 μT) and the downfield APT effects in the tumors were stronger than the upfield NOE, as reported previously (26, 41). However, the contralateral region had negative MTR_{asym}(3.5ppm) signal intensity (−1.74 ± 0.76%). As far as image contrast is concerned, the tumor xenograft showed large, positive MTR_{asym}(3.5ppm) image contrast (5.87 ± 1.01%) in the tumor region, compared to the contralateral region. Moreover, it is particularly important to note that most MTR_{asym}(3.5ppm) image contrasts (about 80.6%) in the tumor region were dominated by the $APT^{\#}$ contrasts, rather than the $NOE^{\#}$.

Figure 4 shows Pearson's correlation analysis results between two measured tissue parameters (T_{1w}, water content), as well as between the measured CEST-MRI signal intensities ($APT^{\#}$, $NOE^{\#}$, or MTR_{asym}(3.5ppm)) and T_{1w}/[water proton]. It can be seen that the T_{1w} values showed a significant, very strong positive correlation with the water content (Pearson's correlation coefficient, $r = 0.7768$; $p = 0.0001$), as reported before (50, 51). The $APT^{\#}$ and MTR_{asym}(3.5ppm) signal intensity values were largely higher in the tumor region than in the contralateral region, while the $NOE^{\#}$ signal intensity values were quite similar for these two regions. Notably, all measured $APT^{\#}$, $NOE^{\#}$, and MTR_{asym}(3.5ppm) signal intensities showed insignificant, negligible correlations with the combined tissue parameter, T_{1w}/[water proton] (all $r < 0.1376$; all $p > 0.5799$).

Figure 5 shows the T_2-weighted MR image and quantitative multi-parametric MR maps for representative rat. The tumor region (compared to the contralateral region) showed hyperintensities on the ADC, CBF, T_{2w}^{obs}, T_{1w}^{obs}, T_{1w}, water content, $APT^{\#}$, and MTR_{asym}(3.5ppm) maps. Consistent with Fig. 3, the tumor region can clearly be identified from $APT^{\#}$ and MTR_{asym}(3.5ppm) maps (hyperintensity region). However, the $NOE^{\#}$ maps

showed negligible image contrasts in tumor region, compared to the contralateral region. Notably, the T_{1w}/[water proton] maps showed negligible image contrasts between the contralateral and the tumor regions. Table 2 summarizes the quantitative analysis results of multi-parametric MRI signal intensities. Consistent with Figs. 3–5, there were significantly large differences between contralateral and tumor regions in all parametric values ($p < 0.05$), except for T_{1w}/[water proton] and NOE$^{\#}$.

DISCUSSION

In this paper, the recently introduced EMR approach (43, 44), based on Henkelman's two-pool MT theory, was applied to the quantification of APT and NOE effects in a rat tumor model, and the correlations between the quantified APT (APT$^{\#}$) and NOE (NOE$^{\#}$) signal intensities and tissue parameters were quantitatively assessed. The Henkelman's two-pool MT model, combined with the super-Lorentzian lineshape for semi-solid protons, has been widely used to describe the semi-solid MT phenomenon in tissue (47, 48). Because the two-pool MT model parameters were fitted using only the one-sided, wide-offset Z-spectrum data (+15 ~ +7 ppm) acquired experimentally (Fig. 2), the downfield CEST and upfield NOE effects in the offset frequency range (+6.5 ~ −15 ppm) were minimized in the obtained EMR signals. The EMR approach could thus measure the pure APT and NOE effects in a more accurate and straightforward manner.

It is important to note that we assumed that the fitted offset range (15ppm ~ 7 ppm) in the EMR approach had no contributions from various CEST and NOE effects. However, these mobile to relatively mobile molecular CEST and NOE effects always have some frequency widths, and their presence may extend into 7 ppm and even further. Therefore, a small fitting deviation at the smaller frequency offset side (~7 ppm) may be seen, as shown in Fig. 2, reflecting the presence of some extended CEST (or even NOE) effects and, thus, affecting the fitting accuracy of the EMR signals. Further, it is known that the observed Z-spectrum is somewhat asymmetric (2, 3), due to the presence of some relatively less mobile biomolecules with a RF saturation width of tens of ppm (41). Thus, when the symmetric MT model-based EMR method is used, the symmetrical semi-solid MT effect is removed, and all others remain. The quantified APT$^{\#}$ signal is almost pure, but the quantified NOE$^{\#}$ signal includes both the local NOE (from mobile biomolecules) component and the conventional MTR_{asym} component (from relatively less mobile biomolecules). Finally, it should be noted that there is currently no gold-standard method which gives accurate APT and NOE values, although we believe that APT$^{\#}$ and NOE$^{\#}$ are in principle more accurate, as discussed in our previous papers (43, 44).

Based on our quantitative results (Fig. 5 and Table 2), the tumor region had higher ADC, water T_2, water T_1, water content, APT$^{\#}$, and MTR_{asym}(3.5ppm) values than the contralateral normal brain region. In several previous APT-MRI studies using the MTR_{asym}(3.5ppm) method at 4.7 T, relatively small APT-weighted signal intensities in tumor region (4.11% for 9L gliosarcoma (2), ~3% for U87 tumor (26, 52)) were reported. Thus, it has been generally accepted that the APT effect in tumor is a few percentages of the water signal intensity. However, the measured signal intensities of APT$^{\#}$ (which were less contaminated by the NOE effects) in the tumor region were actually as large as 11.06%,

which were much larger than the values expected. In Table 2, we simply assumed that the contralateral amide concentration was 71.9 mM, based on the previous literature (3), and calculated the tumor amide concentration. If Eq. [3] is completely correct, these amide proton concentrations should be re-calculated according to the newly measured $APT^{\#}$ values, and the new concentration values would be much larger.

The fact that the $APT^{\#}$ contrast between the tumor and the contralateral region is most dominant at 3.5 ppm and close to zero for wide offsets from 8 to 15 ppm, while the $NOE^{\#}$ contrast is small at 3.5 ppm and increases with frequency offsets (> 5 ppm) clearly shows that the MTR_{asym} contrast mechanism at 3.5 ppm is unique from that for the wide offsets from 8 to 15 ppm. The MTR_{asym} contrast at 3.5 ppm between the tumor and the contralateral region was dominated (about 80.6%) by the downfield large $APT^{\#}$ difference, and the MTR_{asym} contrast for the wide offsets from 8 to 15 ppm was dominated by the upfield $NOE^{\#}$. Notably, the $NOE^{\#}$(3.5ppm) or MTR'_{asym}(3.5ppm) contrast is much smaller than the $NOE^{\#}$ or MTR'_{asym} contrast for the wide offsets from 8 to 15 ppm. In a recent study at 3 T (53), Scheidegger et al. ignored this difference in the MTR'_{asym} contrast and, basing on the MTR'_{asym} contrast at 20 ppm, concluded the MTR'_{asym} contrast to be a major contributor to the MTR_{asym} contrast at 3.5 ppm, which was not a good guess.

As described in our early studies (2, 3), the APT effect in tissue is primarily related to the mobile amide proton content and the amide proton exchange rate in many diseases, such as brain tumors and strokes, although several other tissue and experimental parameters may contribute. In particular, according to Eq. [3], it seems that the APT effect in tissue may be related to the water proton content and the water longitudinal relaxation time (T_{1w}) in tissue. Our study demonstrated that both the water content and the T_{1w} increased in the tumor region (Table 2), compared to the normal brain tissue, consistent with several early studies (50, 51). However, our quantitative results revealed that T_{1w}/[water proton] remained nearly unchanged in the U87 tumor. This means that the effect of the increasing T_{1w} on the measured APT signals was mostly canceled out by the effect of the increasing water content in the tumor xenograft at 4.7 T. Indeed, our correlation analysis results (Fig. 4) indicated that there were no significant correlations between $APT^{\#}$, $NOE^{\#}$, or MTR_{asym}(3.5ppm) signals and T_{1w}/[water proton] in the tumor xenograft. These quantitative measurement results have clearly shown that it is actually unnecessary to correct for the influence of T_{1w} on APT and NOE imaging of gliomas. In a few recent studies at 9.4 T (using the 9L tumor model) and 7 T (using human gliomas), two very different, inverse Z-spectrum (1/Z)-based quantitative metrics (MTR_{Rex} and AREX) were introduced (54, 55). These authors used MTR_{Rex} (defined as the subtraction of the inverse Z-values) to correct for the effects of spillover and semi-solid magnetization transfer, and AREX (= $MTR_{Rex} \cdot R_{1w}$) to further correct for the T_{1w} effect. Indeed, the MTR_{Rex} method can restore the diluted effects of spillover and semi-solid magnetization transfer. However, the effects of the increasing T_{1w} and the increasing water content on the APT measurements may actually mostly be canceled out in many diseases (50, 51). The fact that the influence of T_{1w} on APT imaging *in vivo* is not as being linear as it appears in Eq. [3] led to the unexpected result ($AREX_{tumor} \approx AREX_{normal}$) in the AREX method (simply multiplying by R_{1w} to correct for the T_{1w} effect), as pointed out in our recent study (56).

It is important to assess how the observed APT or APT-weighted hyperintensities in the tumor, compared to the normal brain tissue, are related to the increased mobile amide proton content or the increased amide proton exchange rate (a parameter that depends on tissue pH) in the tumor. Based on previous ^{31}P NMR spectroscopy studies in experimental brain tumors and in patients with brain tumors (57–59), the intracellular pH of untreated malignant gliomas was near neutrality, or a little alkaline (with a slight increase of 0.05–0.08 pH unit reported). The amide proton exchange rate is base-catalyzed in the physiological pH range, and thus, increases exponentially with tissue pH. According to Eq. [3], the quantified amide proton concentration would be decreased if the intracellular pH value indeed increases, or *vice versa*. Based on our quantitative analysis results (Table 2), the APT or APT-weighted contrasts between the tumors and the normal brain tissue are usually dominated by the increased amide proton concentration in the tumors, but an extra contribution from the possibly alkaline intracellular pH may exist.

Finally, based on our EMR method, the large APT$^{\#}$ signal at 3.5 ppm downfield from water, the amine CEST$^{\#}$ signal at 2 ppm downfield from water, and the large NOE$^{\#}$ signal at roughly −3.5 ppm upfield from water were observed in the tumor-related regions, consistent with the Z-spectrum fit with multiple Lorentzian lineshapes at ultrahigh B_0 magnetic fields (>7 T) (60, 61). In several recent CEST studies at ultrahigh B_0 fields (7 T or higher), multiple other endogenous CEST and NOE signals have been observed, such as glutamate CEST at 3 ppm (8, 9), myo-inositol CEST at 0.6 ppm (62), and NOE at −1.6 ppm (63). Although our quantification results (APT$^{\#}$ and NOE$^{\#}$) at 4.7 T may be contaminated by these extra signals, the contributions should be very small or negligible, based on the calculated APT$^{\#}$ and NOE$^{\#}$ signal features plotted as a function of frequency offsets (Fig. 2). Further, the NOE signal from aromatic protons in an offset range of 1 to 5 ppm downfield from water may also exist in the observation (64, 65). However, similar to the aliphatic NOE, the aromatic NOE contrast at 3.5 ppm downfield from water between the tumor and contralateral region should be very small or negligible.

CONCLUSIONS

The results of this study (Figs. 2 and 3) indicated that the pure APT$^{\#}$ signal intensities in the tumor were much larger than the values reported in the literature and were significantly higher than those in the contralateral. Based on the definition (Eq. [1]), the absolute APT-weighted signal intensities measured were reduced by the NOE effect, but remained positive, because the APT$^{\#}$ signals were all larger than the NOE$^{\#}$ signals at this relatively larger RF power (≤1.3 μT). Notably, the MTR_{asym}(3.5ppm) image contrast between the tumor and contralateral regions was actually increased by the presence of the NOE (a positive confounding factor). Moreover, the APT$^{\#}$ signal intensities were generally the major contributor to the observed MTR_{asym}(3.5ppm) image contrast. Our further quantitative analysis results (Fig. 4 and Table 2) showed that both the water content ([water proton]) and water T_1 (T_{1w}) were increased in the tumor xenograft study. However, the effects of the changes in these two tissue parameters on APT imaging were nearly canceled out in this tumor. Notably, the observed APT$^{\#}$ and MTR_{asym}(3.5ppm) hyperintensities in the tumor depended predominantly on increased mobile protein and peptide concentration, with an extra contribution from the possible alkaline intracellular pH, rather than other contribution

factors. Our approach and findings would be helpful for a better understanding of APT and other endogenous CEST imaging contrast mechanisms in malignant tumors and other diseases.

Acknowledgments

The authors thank Dr. Antonella Mangraviti and Dr. Bachchu Lal for preparing animal models and Ms. Mary McAllister for editorial assistance. This work was supported in part by grants from the National Institutes of Health (R01EB009731, R01CA166171, R01NS083435, R01EB015032, R21EB015555, and P41EB015909).

References

1. Ward KM, Aletras AH, Balaban RS. A new class of contrast agents for MRI based on proton chemical exchange dependent saturation transfer (CEST). J Magn Reson. 2000; 143:79–87. [PubMed: 10698648]
2. Zhou JY, Lal B, Wilson DA, Laterra J, van Zijl PCM. Amide proton transfer (APT) contrast for imaging of brain tumors. Magn Reson Med. 2003; 50:1120–1126. [PubMed: 14648559]
3. Zhou JY, Payen JF, Wilson DA, Traystman RJ, van Zijl PCM. Using the amide proton signals of intracellular proteins and peptides to detect pH effects in MRI. Nature Medicine. 2003; 9:1085–1090.
4. Jones CK, Schlosser MJ, van Zijl PCM, Pomper MG, Golay X, Zhou JY. Amide proton transfer imaging of human brain tumors at 3T. Magn Reson Med. 2006; 56:585–592. [PubMed: 16892186]
5. Jin T, Wang P, Zong XP, Kim SG. Magnetic resonance imaging of the Amine-Proton EXchange (APEX) dependent contrast. NeuroImage. 2012; 59:1218–1227. [PubMed: 21871570]
6. Ling W, Regatte RR, Navon G, Jerschow A. Assessment of glycosaminoglycan concentration in vivo by chemical exchange-dependent saturation transfer (gagCEST). Proc Natl Acad Sci (USA). 2008; 105:2266–2270. [PubMed: 18268341]
7. Singh A, Cai KJ, Haris M, Hariharan H, Reddy R. On B1 inhomogeneity correction of in vivo human brain glutamate chemical exchange saturation transfer contrast at 7T. Magn Reson Med. 2013; 69:818–824. [PubMed: 22511396]
8. Cai KJ, Haris M, Singh A, Kogan F, Greenberg JH, Hariharan H, Detre JA, Reddy R. Magnetic resonance imaging of glutamate. Nature Med. 2012; 18:302–306. [PubMed: 22270722]
9. Kogan F, Singh A, Debrosse C, Haris M, Cai KJ, Nanga RP, Elliott M, Hariharan H, Reddy R. Imaging of glutamate in the spinal cord using GluCEST. NeuroImage. 2013; 77:262–267. [PubMed: 23583425]
10. Haris M, Singh A, Cai KJ, Kogan F, McGarvey J, DeBrosse C, Zsido GA, Witschey WRT, Koomalsingh K, Pilla JJ, Chirinos JA, Ferrari VA, Gorman JH, Hariharan H, Gorman RC, Reddy R. A technique for in vivo mapping of myocardial creatine kinase metabolism. Nature Med. 2014; 20:209–214. [PubMed: 24412924]
11. Zhang SR, Winter P, Wu KC, Sherry AD. A novel europium(III)-based MRI contrast agent. J Am Chem Soc. 2001; 123:1517–1518. [PubMed: 11456734]
12. Aime S, Delli Castelli D, Fedeli F, Terreno E. A paramagnetic MRI-CEST agent responsive to lactate concentration. J Am Chem Soc. 2002; 124:9364–9365. [PubMed: 12167018]
13. Li AX, Wojciechowski F, Suchy M, Jones CK, Hudson RHE, Merton RS, Bartha R. A sensitive PARACEST contrast agent for temperature MRI: EU3+-DOTAM-Glycine (Gly)-Phenylalanine (Phe). Magn Reson Med. 2008; 59:374–381. [PubMed: 18228602]
14. Aime S, Calabi L, Biondi L, De Miranda M, Ghelli S, Paleari L, Rebaudengo C, Terreno E. Iopamidol: Exploring the potential use of a well-established X-ray contrast agent for MRI. Magn Reson Med. 2005; 53:830–834. [PubMed: 15799043]
15. Chen LQ, Howison CM, Jeffery JJ, Robey IF, Kuo PH, Pagel MD. Evaluations of Extracellular pH within In Vivo Tumors Using acidoCEST MRI. Magn Reson Med. 2014; 72:1408–1417. [PubMed: 24281951]

16. Chan KWY, McMahon MT, Kato Y, Liu GS, Bulte JWM, Bhujwalla ZM, Artemov D, van Zijl PCM. Natural D-glucose as a biodegradable MRI contrast agent for detecting cancer. Magn Reson Med. 2012; 68:1764–1773. [PubMed: 23074027]
17. Walker-Samuel S, Ramasawmy R, Torrealdea F, Rega M, Rajkumar V, Johnson SP, Richardson S, Gonçalves M, Parkes HG, Årstad E, Thomas D, Pedley RB, Lythgoe MF, Golay X. In vivo imaging of glucose uptake and metabolism in tumors. Nature Med. 2013; 19:1067–1072. [PubMed: 23832090]
18. Rivlin M, Horev J, Tsarfaty I, Navon G. Molecular imaging of tumors and metastases using chemical exchange saturation transfer (CEST) MRI. Sci Reports. 2013:3.
19. Jin T, Mehrens H, Hendrich KS, Kim SG. Mapping brain glucose uptake with chemical exchange-sensitive spin-lock magnetic resonance imaging. Journal of Cerebral Blood Flow and Metabolism. 2014; 34:1402–1410. [PubMed: 24865996]
20. Wen ZB, Hu SG, Huang FH, Wang XL, Guo LL, Quan XY, Wang SL, Zhou JY. MR imaging of high-grade brain tumors using endogenous protein and peptide-based contrast. NeuroImage. 2010; 51:616–622. [PubMed: 20188197]
21. Jia GA, Abaza R, Williams JD, Zynger DL, Zhou JY, Shah ZK, Patel M, Sammet S, Wei L, Bahnson RR, Knopp MV. Amide Proton Transfer MR Imaging of Prostate Cancer: A Preliminary Study. J Magn Reson Imag. 2011; 33:647–654.
22. Dula AN, Arlinghaus LR, Dortch RD, Dewey BE, Whisenant JG, Ayers GD, Yankeelov TE, Smith SA. Amide proton transfer imaging of the breast at 3 T: Establishing reproducibility and possible feasibility assessing chemotherapy response. Magn Reson Med. 2013; 70:216–224. [PubMed: 22907893]
23. Zhou J, Zhu H, Lim M, Blair L, Quinones-Hinojosa A, Messina AA, Eberhart CG, Pomper MG, Laterra J, Barker PB, van Zijl PCM, Blakeley JO. Three-dimensional amide proton transfer MR imaging of gliomas: Initial experience and comparison with gadolinium enhancement. J Magn Reson Imag. 2013; 38:1119–1128.
24. Togao O, Yoshiura T, Keupp J, Hiwatashi A, Yamashita K, Kikuchi K, Suzuki Y, Suzuki SO, Iwaki T, Hata N, Mizoguchi M, Yoshimoto K, Sagiyama K, Takahashi M, Honda H. Amide proton transfer imaging of adult diffuse gliomas: correlation with histopathological grades. Neuro-Oncology. 2014; 16:441–448. [PubMed: 24305718]
25. Zhou J, Tryggestad E, Wen Z, Lal B, Zhou T, Grossman R, Wang S, Yan K, Fu D-X, Ford E, Tyler B, Blakeley J, Laterra J, van Zijl PCM. Differentiation between glioma and radiation necrosis using molecular magnetic resonance imaging of endogenous proteins and peptides. Nature Med. 2011; 17:130–134. [PubMed: 21170048]
26. Hong X, Liu L, Wang M, Ding K, Fan Y, Ma B, Lal B, Tyler B, Mangraviti A, Wang S, Wong J, Laterra J, Zhou J. Quantitative multiparametric MRI assessment of glioma response to radiotherapy in a rat model. Neuro-Oncology. 2014; 16:856–867. [PubMed: 24366911]
27. Sagiyama K, Mashimo T, Togao O, Vemireddy V, Hatanpaa KJ, Maher EA, Mickey BE, Pan E, Sherry AD, Bachoo RM, Takahashi M. In vivo chemical exchange saturation transfer imaging allows early detection of a therapeutic response in glioblastoma. Proc Natl Acad Sci (USA). 2014; 111:4542–4547. [PubMed: 24616497]
28. Hectors S, Jacobs I, Strijkers GJ, Nicolay K. Amide proton transfer imaging of high intensity focused ultrasound-treated tumor tissue. Magn Reson Med. 2014; 72:1113–1122. [PubMed: 24154945]
29. Sun PZ, Zhou J, Sun W, Huang J, van Zijl PCM. Detection of the ischemic penumbra using pH-weighted MRI. J Cereb Blood Flow Metab. 2007; 27:1129–1136. [PubMed: 17133226]
30. Zhao X, Wen Z, Huang F, Lu S, Wang X, Hu S, Zu D, Zhou J. Saturation power dependence of amide proton transfer image contrasts in human brain tumors and strokes at 3 T. Magn Reson Med. 2011; 66:1033–1041. [PubMed: 21394783]
31. McVicar N, Li AX, Goncalves DF, Bellyou M, Meakin SO, Prado MA, Bartha R. Quantitative tissue pH measurement during cerebral ischemia using amine and amide concentration-independent detection (AACID) with MRI. J Cereb Blood Flow Metab. 2014; 34:690–698. [PubMed: 24496171]

32. Tee YK, Harston GW, Blockley N, Okell TW, Levman J, Sheerin F, Cellerini M, Jezzard P, Kennedy J, Payne SJ, Chappell MA. Comparing different analysis methods for quantifying the MRI amide proton transfer (APT) effect in hyperacute stroke patients. NMR Biomed. 2014; 27:1019–1029. [PubMed: 24913989]
33. Tietze A, Blicher J, Mikkelsen IK, Ostergaard L, Strother MK, Smith SA, Donahue MJ. Assessment of ischemic penumbra in patients with hyperacute stroke using amide proton transfer (APT) chemical exchange saturation transfer (CEST) MRI. NMR Biomed. 2014; 27:163–174. [PubMed: 24288260]
34. Harston GW, Tee YK, Blockley N, Okell TW, Thandeswaran S, Shaya G, Sheerin F, Cellerini M, Payne S, Jezzard P, Chappell M, Kennedy J. Identifying the ischaemic penumbra using pH-weighted magnetic resonance imaging. Brain. 2015; 138:36–42. [PubMed: 25564491]
35. Zhou J, Blakeley JO, Hua J, Kim M, Laterra J, Pomper MG, van Zijl PCM. Practical data acquisition method for human brain tumor amide proton transfer (APT) imaging. Magn Reson Med. 2008; 60:842–849. [PubMed: 18816868]
36. Lee JS, Regatte RR, Jerschow A. Isolating chemical exchange saturation transfer contrast from magnetization transfer asymmetry under two-frequency rf irradiation. J Magn Reson. 2012; 215:56–63. [PubMed: 22237631]
37. Jones CK, Huang A, Xu J, Edden RA, Schar M, Hua J, Oskolkov N, Zaca D, Zhou J, McMahon MT, Pillai JJ, van Zijl PC. Nuclear Overhauser enhancement (NOE) imaging in the human brain at 7T. Neuroimage. 2013; 77:114–124. [PubMed: 23567889]
38. Jin T, Wang P, Zong X, Kim S-G. MR imaging of the amide-proton transfer effect and the pH-insensitive nuclear overhauser effect at 9.4 T. Magn Reson Med. 2013; 69:760–770. [PubMed: 22577042]
39. Liu D, Zhou J, Xue R, Zuo Z, An J, Wang DJJ. Quantitative characterization of nuclear Overhauser enhancement and amide proton transfer effects in the human brain at 7 Tesla. Magn Reson Med. 2013; 70:1070–1081. [PubMed: 23238951]
40. Lu J, Zhou J, Cai C, Cai S, Chen Z. Observation of true and pseudo NOE signals using CEST-MRI and CEST-MRS sequences with and without lipid suppression. Magn Reson Med. 2015; 73:1615–1622. [PubMed: 24803172]
41. Zhou JY, Hong XH, Zhao XN, Gao JH, Yuan J. APT-weighted and NOE-weighted image contrasts in glioma with different RF saturation powers based on magnetization transfer ratio asymmetry analyses. Magn Reson Med. 2013; 70:320–327. [PubMed: 23661598]
42. Zhou JY, Wilson DA, Sun PZ, Klaus JA, van Zijl PCM. Quantitative description of proton exchange processes between water and endogenous and exogenous agents for WEX, CEST, and APT experiments. Magn Reson Med. 2004; 51:945–952. [PubMed: 15122676]
43. Heo H-Y, Zhang Y, Lee D-H, Hong X, Zhou J. Quantitative assessment of amide proton transfer (APT) and nuclear Overhauser enhancement (NOE) imaging with extrapolated semi-solid magnetization transfer reference (EMR) signals: Application to a rat glioma model at 4.7 T. Magn Reson Med. 2015; doi: 10.1002/mrm.25581
44. Heo HY, Zhang Y, Jiang S, Lee DH, Zhou J. Quantitative assessment of amide proton transfer (APT) and nuclear overhauser enhancement (NOE) imaging with extrapolated semisolid magnetization transfer reference (EMR) signals: II. Comparison of three EMR models and application to human brain glioma at 3 Tesla. Magn Reson Med. 2015; doi: 10.1002/mrm.25795
45. Sun PZ, Zhou J, Sun W, Huang J, van Zijl PC. Suppression of lipid artifacts in amide proton transfer imaging. Magn Reson Med. 2005; 54:222–225. [PubMed: 15968669]
46. Kim M, Gillen J, Landman BA, Zhou JY, van Zijl PCM. Water Saturation Shift Referencing (WASSR) for Chemical Exchange Saturation Transfer (CEST) Experiments. Magn Reson Med. 2009; 61:1441–1450. [PubMed: 19358232]
47. Henkelman RM, Huang XM, Xiang QS, Stanisz GJ, Swanson SD, Bronskill MJ. Quantitative Interpretation of Magnetization-Transfer. Magn Reson Med. 1993; 29:759–766. [PubMed: 8350718]
48. Morrison C, Henkelman RM. A Model for Magnetization-Transfer in Tissues. Magn Reson Med. 1995; 33:475–482. [PubMed: 7776877]

49. Ozawa T, Faddegon BA, Hu LJ, Bollen AW, Lamborn KR, Deen DF. Response of intracerebral human glioblastoma xenografts to multifraction radiation exposures. Intern J Rad Oncol Biol Phys. 2006; 66:263–270.
50. Damadian R. Tumor Detection by Nuclear Magnetic Resonance. Science. 1971; 171:1151. [PubMed: 5544870]
51. Saryan LA, Hollis DP, Economou JS, Eggleston JC. Nuclear magnetic resonance studies of cancer. IV. Correlation of water content with tissue relaxation times. J Natl Cancer Inst. 1974; 52:599–602. [PubMed: 4406036]
52. Zhao XN, Wen ZB, Huang FH, Lu SL, Wang XL, Hu SG, Zu DL, Zhou JY. Saturation Power Dependence of Amide Proton Transfer Image Contrasts in Human Brain Tumors and Strokes at 3 T. Magn Reson Med. 2011; 66:1033–1041. [PubMed: 21394783]
53. Scheidegger R, Wong ET, Alsop DC. Contributors to contrast between glioma and brain tissue in chemical exchange saturation transfer sensitive imaging at 3 Tesla. NeuroImage. 2014; 99:256–268. [PubMed: 24857712]
54. Xu JZ, Zaiss M, Zu ZL, Li H, Xie JP, Gochberg DF, Bachert P, Gore JC. On the origins of chemical exchange saturation transfer (CEST) contrast in tumors at 9.4 T. NMR Biomed. 2014; 27:406–416. [PubMed: 24474497]
55. Zaiss M, Windschuh J, Paech D, Meissner JE, Burth S, Schmitt B, Kickingereder P, Wiestler B, Wick W, Bendszus M, Schlemmer HP, Ladd ME, Bachert P, Radbruch A. Relaxation-compensated CEST-MRI of the human brain at 7 T: Unbiased insight into NOE and amide signal changes in human glioblastoma. NeuroImage. 2015; 112:180–188. [PubMed: 25727379]
56. Yan K, Fu Z, Yang C, Zhang K, Jiang S, Lee DH, Heo HY, Zhang Y, Cole RN, Van Eyk JE, Zhou J. Assessing Amide Proton Transfer (APT) MRI Contrast Origins in 9 L Gliosarcoma in the Rat Brain Using Proteomic Analysis. Mol Imaging Biol. 2015; 17:479–487. [PubMed: 25622812]
57. Griffiths JR. Are cancer cells acidic? Br J Cancer. 1991; 64:425–427. [PubMed: 1911181]
58. Maintz D, Heindel W, Kugel H, Jaeger R, Lackner KJ. Phosphorus-31 MR spectroscopy of normal adult human brain and brain tumours. Nmr in Biomedicine. 2002; 15:18–27. [PubMed: 11840549]
59. Ross BD, Higgins RJ, Boggan JE, Knittel B, Garwood M. 31P NMR spectroscopy of the in vivo metabolism of an intracerebral glioma in the rat. Magn Reson Med. 1988; 6:403–417. [PubMed: 3380002]
60. Desmond KL, Moosvi F, Stanisz GJ. Mapping of amide, amine, and aliphatic peaks in the CEST spectra of murine xenografts at 7 T. Magn Reson Med. 2014; 71:1841–1853. [PubMed: 23801344]
61. Cai K, Singh A, Poptani H, Li W, Yang S, Lu Y, Hariharan H, Zhou XJ, Reddy R. CEST signal at 2ppm (CEST@2ppm) from Z-spectral fitting correlates with creatine distribution in brain tumor. NMR Biomed. 2015; 28:1–8. [PubMed: 25295758]
62. Haris M, Cai K, Singh A, Hariharan H, Reddy R. In vivo mapping of brain myo-inositol. NeuroImage. 2011; 54:2079–2085. [PubMed: 20951217]
63. Zu Z, Xu J, Li H, Chekmenev EY, Quarles CC, Does MD, Gore JC, Gochberg DF. Imaging amide proton transfer and nuclear overhauser enhancement using chemical exchange rotation transfer (CERT). Magn Reson Med. 2014; 72:471–476. [PubMed: 24302497]
64. Jin, T., Kim, S-G. In vivo saturation transfer imaging of nuclear Overhauser effect from aromatic and aliphatic protons: implication to APT quantification. Proc 21th Annual Meeting ISMRM; Salt Lake City, Utah. 2013; p. 2528
65. Goerke S, Zaiss M, Kunz P, Klika KD, Windschuh JD, Mogk A, Bukau B, Ladd ME, Bachert P. Signature of protein unfolding in chemical exchange saturation transfer imaging. NMR Biomed. 2015; 28:906–913. [PubMed: 26010522]

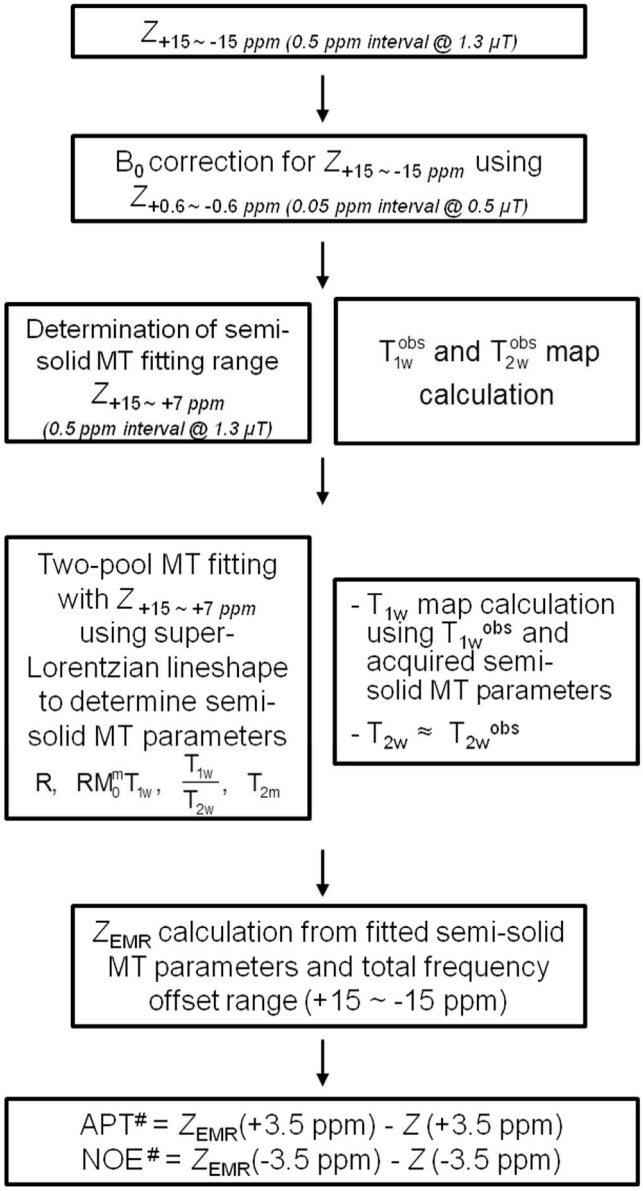

Fig. 1.

Flow chart for APT# and NOE# quantification procedures. The acquired Z-spectrum was subject to the B_0 correction using WASSR or other methods. The limited Z-spectrum dataset with positive, large frequency offsets (to avoid possible CEST and NOE effects) and calculated T_{1w}^{obs} and T_{2w}^{obs}, based on additional relaxation time measurement experiments, were used to fit the two-pool MT model parameters. Z_{EMR} spectra were calculated by the fitted MT model parameters. Finally, the APT# and NOE# signals were calculated by subtracting Z_{EMR} and experimentally acquired data at 3.5 and −3.5 ppm, respectively. All procedures were performed on the basis of ROI or pixel-by-pixel.

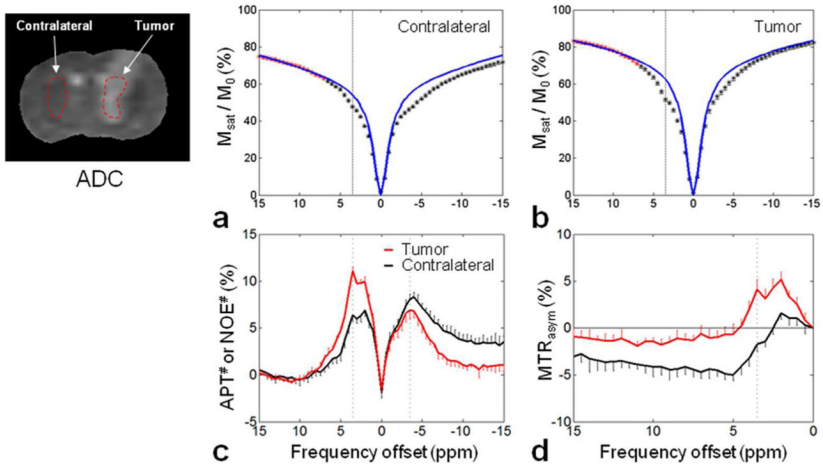

Fig. 2.

Experimentally acquired Z-spectra (black and red asterisks) and calculated Z_{EMR} spectra (blue lines) for the contralateral (a) and the tumor (b) brain regions. For each ROI, the limited Z-spectrum dataset with positive, large frequency offsets (red asterisks) was used for the two-pool MT model fitting. Calculated $APT^{\#}$, $NOE^{\#}$ (c) and MTR_{asym}(3.5ppm) (d) signal features as a function of frequency offsets for the contralateral (black line) and the tumor (red line) regions. The $APT^{\#}$ and $NOE^{\#}$ results were obtained by subtracting the experimentally acquired Z-spectra from the corresponding calculated EMR spectra, and the MTR_{asym}(3.5ppm) results were obtained by subtracting the experimental Z-spectra on the positive offset side from the experimental Z-spectra on the negative offset side. All spectra were represented with standard errors.

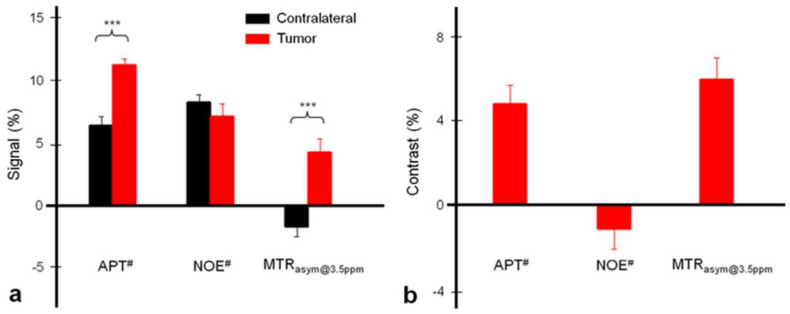

Fig. 3.

(a) Calculated APT$^{\#}$, NOE$^{\#}$, and MTR$_{asym}$(3.5ppm) signal intensities. (b) Calculated corresponding image contrasts using signal intensity differences between the tumor and contralateral brain regions. Error bars depict standard errors. The statistical significance of the signal intensity difference compared with the contralateral brain region for each group: * $p < 0.05$, *** $p < 0.001$, not marked = not significant.

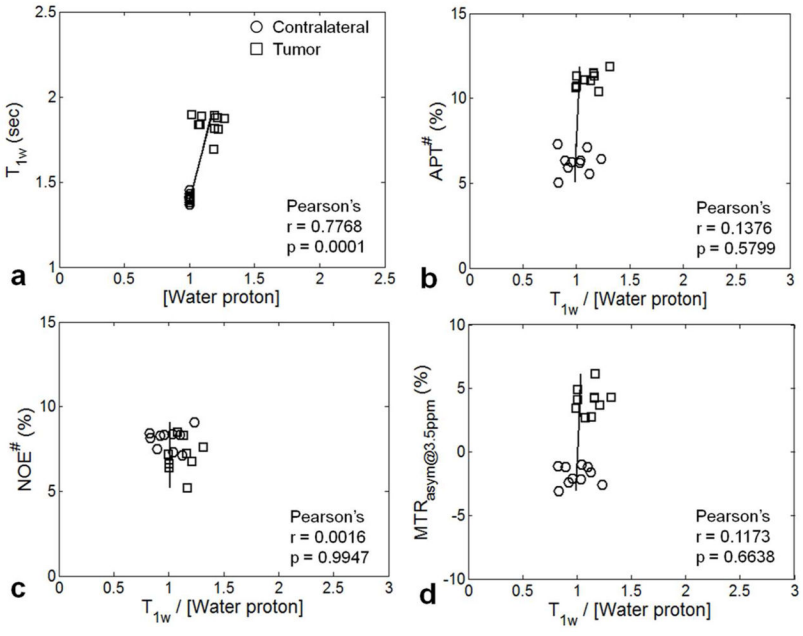

Fig. 4.

Pearson's correlation analysis results (n = 11). (a) T_{1w} versus water content. (b) $APT^{\#}$ signal intensities versus T_{1w}/[water proton]. (c) $NOE^{\#}$ signal intensities versus T_{1w}/[water proton]. (d) MTR_{asym} signal intensities versus T_{1w}/[water proton]. The black lines indicate the linear regression of all ROI values. The Pearson's correlation coefficients (r) and p values were calculated in each correlation graph.

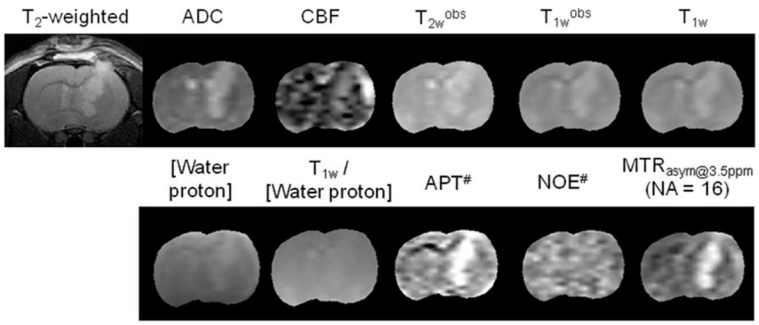

Fig. 5.

Acquired T_2-weighted MR images and calculated quantitative multi-parametric MR maps for a four representative rat. The display windows are: ADC (0.5 ~ 2 × 10^{-9} m^2/sec); CBF (0 ~ 200 mL/100g/min); T_{2w}^{obs} (0 ~ 100 msec); T_{1w}^{obs} and T_{1w} (0 ~ 3 sec); T_{1w}/[water proton] (0 ~ 3); $APT^{\#}$ and $NOE^{\#}$ (0 ~ 15%); and MTR_{asym}(3.5ppm) (−6% ~ 6%).

Table 1

Fitted two-pool semi-solid MT model parameters (mean ± standard error)

	R (sec^{-1})	$RM_{0m}T_{1w}$	T_{1w}/T_{2w}	T_{2m} (μsec)	R^2 (%)
Contralateral	44.75 ± 2.49	4.90 ± 0.19	22.93 ± 0.44	18.21 ± 1.39	94.22 ± 0.73
Tumor	49.98 ± 0.03	3.20 ± 0.19	25.45 ± 0.97	19.89 ± 0.24	95.76 ± 0.36

Table 2

Calculated quantitative multi-parametric signal intensities (mean ± standard error)

	ADC (m^2/sec)	CBF (ml/100g/min)	T_{2w}^{obs} (msec)	T_{1w}^{obs} (sec)	T_{1w} (sec)	[Water proton]$^{\$}$	T_{1w}/[Water proton]$^{\$}$	APT$^{\#}$ (%)	NOE$^{\#}$ (%)	MTR_{asym} (3.5ppm) (%)	[Amide proton]$^{!}$ (mM)
Contralateral	0.92 ± 0.02	58.4 ± 15.7	56.47 ± 0.99	1.36 ± 0.02	1.40 ± 0.02	1	1	6.33 ± 0.68	8.08 ± 0.56	−1.74 ± 0.76	71.9
Tumor	1.25 ± 0.04	80.06 ± 36.3	72.29 ± 3.05	1.79 ± 0.05	1.84 ± 0.06	1.19 ± 0.13	1.09 ± 0.13	11.06 ± 0.46	6.93 ± 1.04	4.12 ± 1.02	110.2 ± 16.2 $^{(+0.1)}$ 138.8 ± 20.3 174.9 ± 25.2 $^{(-0.1)}$

$^{\$}$The contralateral [water proton] and T_{1w}/[water proton] values were set to 1.

$^{!}$The contralateral amide proton concentration value was taken from the literature (3), and the degree of amide proton concentration variations in the tumor due to intracellular pH was assessed using an increase or decrease of 0.1 pH unit.